

Quantification of bone marrow interstitial pH and calcium concentration by intravital ratiometric imaging

Shu-Chi Yeh

Massachusetts General Hospital

Jue Hou

Massachusetts General Hospital

Juwell Wu

Massachusetts General Hospital

Fernando Camargo

Boston Children's Hospital <https://orcid.org/0000-0002-5630-5909>

Charles Lin (✉ charles.lin@hms.harvard.edu)

Massachusetts General Hospital

Article

Keywords: hematopoietic stem cells (HSCs), bone marrow interstitial pH, calcium concentration, intravital ratiometric imaging

Posted Date: February 19th, 2021

DOI: <https://doi.org/10.21203/rs.3.rs-237943/v1>

License:  This work is licensed under a Creative Commons Attribution 4.0 International License.

[Read Full License](#)

Version of Record: A version of this preprint was published at Nature Communications on January 19th, 2022. See the published version at <https://doi.org/10.1038/s41467-022-27973-x>.

Title

Quantification of bone marrow interstitial pH and calcium concentration by intravital ratiometric imaging

Authors

S-C. A. Yeh ^{1,†}, J. Hou ^{1,†}, J. W. Wu ¹, F. D. Camargo ^{2,3}, C. P. Lin ^{1,4,*}.

Affiliations

¹Advanced Microscopy Program, Center for Systems Biology and Wellman Center for Photomedicine, and Center for Regenerative Medicine, Massachusetts General Hospital, Harvard Medical School, Boston, MA, 02114, USA.

²Stem Cell Program, Boston Children's Hospital, Boston, MA, USA

³Department of Stem Cell and Regenerative Biology, Harvard University, Cambridge, MA, USA

⁴Harvard Stem Cell Institute, Harvard University, Cambridge, MA, 02138, USA.

†Co-first author

*Corresponding author

Contact Information

Email: charles.lin@hms.harvard.edu

Abstract

The fate of hematopoietic stem cells (HSCs) in the bone marrow can be directed by microenvironmental factors including extracellular calcium ion concentration ($[Ca^{2+}]_e$). $[Ca^{2+}]_e$ can vary significantly with bone remodeling, but the local $[Ca^{2+}]_e$ around individual HSCs *in vivo* remains unknown. Here we developed an intravital ratiometric imaging approach to quantify the absolute pH and $[Ca^{2+}]_e$ in the mouse calvarial bone marrow, taking into account the pH sensitivity of the calcium probe and the wavelength-dependent optical loss through bone to ensure unbiased ratiometric analyses. We uncovered substantial heterogeneity in $[Ca^{2+}]_e$ (1.0 - 3.6 mM) surrounding steady-state HSCs. While the lowest $[Ca^{2+}]_e$ (0.3 mM) was found in regions dominated by bone formation, HSCs were not found in those locations. This work thus established a tool to further investigate $[Ca^{2+}]_e$ and pH in the HSC niche under malignant or stressed conditions and can be broadly applied to other tissue types.

INTRODUCTION

Hematopoietic stem cells (HSCs) reside in the bone marrow (BM), long considered to be a compartment that is rich in calcium, particularly near the endosteal surface bordering the bone and the BM¹. In adult mammals, 99% of the calcium is stored in the skeleton, which undergoes constant remodeling through cycles of bone resorption and new bone deposition². In contrast to the tightly regulated calcium ion concentration ($[Ca^{2+}]$) in the blood serum with a setpoint near 2 mM^{3–5}, the local extracellular calcium concentration ($[Ca^{2+}]_e$) at the endosteal surface can reach as high as 40 mM at sites of bone resorption, and the difference may help to specify the BM as the destination for HSC homing during development and after systemic transplantation¹. HSCs respond to extracellular calcium through the calcium sensing receptor (CaR), and fetal liver HSCs lacking the CaR showed defective engraftment in the BM as they are unable to home properly to the endosteal niche¹. A very different view of calcium in the HSC niche; however, was presented recently by Luchsinger et al., who reported that low extracellular calcium (0.02 – 0.2 mM) enhanced HSC maintenance *in vitro* through calpain protease inhibition. In addition, an average $[Ca^{2+}]_e$ of 0.5 mM was found in BM interstitial fluid extracted from tibia, much lower than serum calcium, suggesting that HSCs are maintained in a BM microenvironment with low $[Ca^{2+}]_e$ ^{3,6}. These conflicting observations highlight the need to further examine the role of extracellular calcium in regulating the fate and function of HSCs *in vivo*. Our recent finding⁷ that diverse remodeling stages across multitude of BM cavities differentially support HSC expansion after stimulation further raises the question whether varying local calcium levels contribute to HSC niche heterogeneity. However, the spatial distribution of calcium ions in the physiological microenvironment is largely unknown as there is currently no tool available to probe interstitial calcium at cellular resolution *in vivo*.

Early attempts to quantify $[Ca^{2+}]_e$ used either neutral ligand or organophosphate based calcium-selective microelectrode^{8,9}. The method has been used to measure the $[Ca^{2+}]_e$ in intact gastric mucosa explant, hair cells and central nervous system, with the baseline $[Ca^{2+}]_e$ in the rat cerebellum reported to be around 1.0 – 1.2 mM¹⁰. In an elegant experiment, Silver et al measured the $[Ca^{2+}]_e$ in the bone resorption pit by inserting the ion electrode tip underneath the osteoclasts in a rabbit ear chamber model implanted with bone fragments and obtained readings as high as 40 mM. As acidification is required for dissolving the bone mineral, the pH in the bone resorption pit was also measured in the same experiment and found to be as low as 4.7. The method, though quantitative, is invasive and only provided $[Ca^{2+}]_e$ and pH readings at discrete locations in tissue¹¹.

Spatial distribution of $[Ca^{2+}]_e$ can be assessed by quantitative imaging based on calcium sensitive ratiometric probes^{12–14}. When combined with laser-scanning microscopy, it allows calcium measurements with high spatial and temporal resolution^{15,16}. However, commercially available ratiometric probes are only suitable for detecting $[Ca^{2+}]_e$ up to hundreds of μM . Although intensity-based indicators for detecting $[Ca^{2+}]_e$ in the mM range are under development^{17,18}, and relative $[Ca^{2+}]_e$ changes have been reported in brain tissue using Rhod-5N¹⁹, absolute quantification requires ratiometric analysis to overcome the limitation of intensity-based measurements (subject to variations in local fluorophore concentrations and tissue optical properties). Moreover, as calcium indicators are sensitive to proton densities, information on the pH distribution is also needed for proper determination of tissue $[Ca^{2+}]_e$ ²⁰.

In this work, we developed an intravital imaging approach to quantify the absolute pH distribution and $[Ca^{2+}]$ in the native BM of mouse calvarium. We employed commercially available probes, SNARF-1 and Rhod-5N, for two-photon imaging of pH and calcium, respectively. As Rhod-5N is not a ratiometric probe, we further paired it with Alexa Fluor 488 (AF488) as a reference dye. We found that the apparent fluorescence ratio changes with imaging depth due to the fact that the bone is a highly scattering tissue, and corrections are required to account for the

wavelength-dependent light attenuation in order to recover the accurate ratio. With appropriate corrections, we were able to map the pH and $[Ca^{2+}]_e$ distribution *in vivo* both in the intravascular and the interstitial space of the BM, with the interstitial pH ranging from 6.8 to 7.4 and $[Ca^{2+}]_e$ from 0.3 – 4.4 mM. In addition, we found different levels of interstitial calcium in BM cavities undergoing distinct stages of bone remodeling, with the lowest $[Ca^{2+}]_e$ measured in cavities exhibiting predominantly bone deposition activities. Finally, we showed that long-term (LT)-HSCs reside in perivascular BM locations where the $[Ca^{2+}]_e$ ranged from ~1.0 to 3.6 mM.

RESULTS

Ratiometric imaging of BM pH *in vivo*

Quantification of pH distribution in the BM is critical for accurate determination of calcium concentrations because the dissociation constant (K_d) of Rhod-5N is pH sensitive. To probe the pH distribution, we used SNARF-1, a ratiometric pH indicator, conjugated to 70 kD dextran. Although widely used in other settings, whether ratiometric analyses can reliably provide quantitative information in a highly scattering tissue such as bone has not been adequately tested. To establish the validity of ratiometric imaging for bone tissue, we first examined BM vasculature labeled with SNARF-1. Analyses of 3D stacks acquired using intravital two-photon microscopy of mouse calvarium (Figure 1a and Suppl. Video 1) revealed a consistent red shift in the SNARF-1 fluorescence signal with increasing image depth (Figure 1b). The red shift is unlikely to result from increasing pH with depth since the intravascular pH is expected to remain constant. A more plausible explanation is the wavelength-dependent attenuation of the fluorescence signal, as the green channel decays at a faster rate than the red channel with increasing depth. Therefore, even when imaging through only less than 100 μm of bone tissue, correction of the differential attenuation is necessary to faithfully recover the true red/green (R/G) ratio for signals originating from within the bone.

Attempt to correct for the wavelength-dependent attenuation using a single exponential decay (with separate coefficients for each wavelength) was unsatisfactory (data not shown). We implemented a two-step algorithm to take into account the local bone thickness (Z_1) and the depth into BM (Z_2), respectively (Figure 1c). Photons emitted from a given voxel within the BM will need to traverse a distance Z_2 to reach the endosteal surface (the interface between the BM and the bone), followed by another distance Z_1 to the bone surface before being detected. As the bone surface and the endosteal surface each has a distinct local curvature, Z_1 and Z_2 are not constants but vary from location to location. For each 3D stack, we generated maps of Z_1 and Z_2 (a local bone thickness map and a depth map, Figure 1d) based on the bone second harmonic generation (SHG) signal and derived the two attenuation coefficients from the cortical bone and the BM ($C_{1,2}$) by fitting the fluorescence decay using Eq. 4-6 (see methods). Applying the two correction factors throughout the stack (Suppl. Figure 1, Suppl. Video 2), we recovered the intravascular SNARF-1 fluorescence signal whose R/G ratio is invariant with depth (Figure 1b). By converting the measured ratios to pH based on a calibration curve established *in vitro* (Figure 1e), we obtained a mean intravascular pH of approximately 7.3 (Figure 1f), consistent with the reported blood serum pH for mice under isoflurane anesthesia²¹.

In addition to labeling the intravascular compartment, the SNARF-1-conjugated dextran also displayed a prominent extravascular signal (Figure 1a and Suppl. Video 1) as the dye readily leaked out of the highly permeable BM vasculature within minutes after injection²². Notably, BM cells are visible as dark objects against a bright fluorescent background (negative contrast), a pattern consistent with the dye being sequestered in the interstitial space and not taken up by the majority of BM cells. We generated a digital mask by 3D image segmentation to outline the interstitial space (Suppl. Figure 2) and performed ratiometric analysis within the masked voxels to determine the BM interstitial pH. As shown in Figure 1f, the interstitial pH values ranged from

6.8 – 7.4 (7.0 to 7.2 within 10% to 90% confidence interval), with a mean value of 7.1, slightly more acidic compared to the blood serum but the difference was statistically significant.

Quantification of interstitial calcium concentration in the BM

Next, we examined the spatial distribution of interstitial calcium in the BM using the ratiometric imaging approach established in the previous section. Available ratiometric calcium indicators are however unsuitable for measuring $[Ca^{2+}]_e$ in the BM, expected to be in the mM range and potentially reaching as high as 40 mM near bone resorption sites¹¹, whereas most sensors are designed for intracellular $[Ca^{2+}]$ measurements with nM to μM sensitivity. We employed a commercially available calcium indicator, Rhod-5N that has been shown to have high dissociation constant ($K_d \sim 320 \mu M$ in buffer and up to 4.5 mM in sea water)²³. Because Rhod-5N is not a ratiometric indicator, we paired it with a reference dye AF488 of a similar molecular weight to enable quantitative ratiometric analyses. The two dyes can be imaged simultaneously using a single laser wavelength for two-photon excitation. As shown in Figure 2a and Suppl. Video 3, both Rhod-5N and AF488 are cell-impermeable and readily label the BM interstitial space after intravascular delivery. In addition, we observed discrete regions on the endosteal surface with very bright Rhod-5N signals. These regions were identified as osteoids (new bone matrices that were not yet mineralized) based on the presence of collagen structures that lack bone mineral staining (Suppl. Figure 3). These regions were excluded in the analysis of interstitial calcium distribution.

Similar to pH quantifications, we first confirmed that Rhod-5N/AF488 ratios for intravascular $[Ca^{2+}]$ is independent of image depth after applying the two-step algorithm for local bone thickness and depth correction (Figure 2b-c). We also confirmed that the ratiometric imaging was able to report the $[Ca^{2+}]$ in real time by injecting a calcium chelator (Calcein Blue) while monitoring the transient changes in the Rhod-5N/AF488 ratios (Figure 2d, Suppl. Video 4). Additional control experiments were conducted to ensure that the ratiometric analysis is independent of laser power and absolute dye concentration, as long as the relative concentrations of the two dyes are held constant (Suppl. Figure 4a,b). Although the ratios increased somewhat when the dye mixture was diluted to the extent that the fluorescence intensities dropped to the noise level, the regions of low fluorescence signal were excluded from the analysis by an intensity-based image segmentation algorithm. Finally, to compensate for the slightly different rates of Rhod-5N and AF488 clearance in vivo, we derived local decay coefficients based on fluorescence attenuation over time throughout subregions of 20-by-20 pixels to accommodate spatially varying clearance rates in the BM (Suppl. Figure 4c-d).

In order to convert the measured Rhod5N/AF488 ratios to absolute $[Ca^{2+}]$ (Figure 3a), we performed in vitro calibrations of the Rhod-5N/AF488 responses to $[Ca^{2+}]$ and a range of pH values found in the BM (Figure 1f). The resulting calibration curves (Figure 3b) were used to derive the mean BM intravascular $[Ca^{2+}]$, which was found to be ~2 mM, in agreement with the reported serum $[Ca^{2+}]$. These results were further confirmed using extracted blood serum samples measured in vitro and by the standard Arsenazo III assay (Figure 3c-d). With proper segmentation, we were also able to determine the $[Ca^{2+}]_e$ in the BM by ratiometric imaging (Figure 3a). $[Ca^{2+}]_e$ was found to be significantly different from the serum with a large spread, where the $[Ca^{2+}]_e$ ranges from 0.3 – 4.4 mM (Figure 3c-d).

Distinct interstitial calcium concentrations in BM cavities undergoing different stages of bone remodeling

We next asked whether various stages of bone remodeling could render heterogeneous calcium distribution among BM cavities, as local bone remodeling activity has been found to influence hematopoietic cell behavior within the cavity. To visualize bone remodeling, as detailed by Christodoulou et al.⁷, we administered spectrally distinct bone front stains, one at 48 h before

calcium imaging to label the old bone fronts (Dye1), and one immediately after calcium imaging to stain the new bone fronts (Dye2). By quantifying the fraction of the old bone fronts that has been eroded, we showed that BM cavities are heterogeneous and can be classified into three types undergoing predominately bone resorption (R-type), new bone deposition (D-type), or with mixed resorption and deposition activities (M-type).

Examples of combined bone remodeling and Rhod-5N/AF488 ratiometric imaging for D-, M-, and R-type cavities are shown in Figure 4a. As expected, osteoids were found predominately in D-type cavities. Restricting our analysis to the interstitial space (excluding osteoids), we observed significant Rhod-5N/AF488 ratio differences among cavities (Figure 4b,c and Supp. Videos 5-6). The measured $[Ca^{2+}]_e$ was found to be significantly lower in D-type cavities (mean ~1.5 mM) than M- and R-type cavities (mean ~1.8 mM) that contained regions with bone resorption, whereas there was essentially no difference between M- and R-type cavities.

LT-HSCs are maintained at $[Ca^{2+}]_e$ comparable to the serum level at the steady state

Conflicting reports^{1,3,6} have suggested that HSCs either home to calcium-rich BM locations, or are maintained in a low-calcium microenvironment. Using the recently developed HSC-specific reporter mice⁷ and the ratiometric imaging method described above, we are able to measure the local calcium distribution surrounding individual HSCs in the steady state BM (Figure 4d). Prior to injecting Rhod-5N and AF488, we first identified the BM locations with *MDS*^{GFP/+};*FLT3*^{Cre} (MFG) cells, which mark the most primitive LT-HSC populations⁷. The step ensures unambiguous identification of HSCs as the HSC-GFP signals were easily overwhelmed by the brighter AF488 fluorescence after dye infusion. By analyzing the Rhod-5N/AF488 ratio in a 3-cell-radius neighborhood around the MFG HSCs, we found their local $[Ca^{2+}]_e$ to range from ~1.0 to 3.6 mM (Figure 4c-d). Although BM locations with lower $[Ca^{2+}]_e$ exist, particularly in D-type cavities, native HSCs were not found in those locations (Suppl. Figure 5).

DISCUSSION

Our work here describes the use of intravital imaging to quantify the absolute $[Ca^{2+}]$ and pH in the BM with high spatial resolution. We show that ratiometric imaging can be useful for extracting quantitative information from two-photon-excited fluorescence signals in highly scattering tissues such as bone, provided appropriate steps are taken to correct for the wavelength-dependent light attenuation with imaging depth. Without the correction, the ratios can deviate significantly from their undistorted values (Figure 1b, 2b-c). Absolute quantification is also possible (even preferable) using indicators whose emission lifetime is sensitive to the analyte concentration, thus avoiding the issue of spectral distortion. Two-photon phosphorescence lifetime microscopy was previously used to measure the BM oxygen concentration *in vivo*²⁴. However, the instrumentation for lifetime imaging is considerably more complex, and we are not aware of lifetime-based sensors for measuring $[Ca^{2+}]$.

Another notable advance of the work described here is the image segmentation, which is critical for the delineation of the interstitial space. The BM contains both a high density of blood vessels and a high density of hematopoietic cells. The vasculature occupies ~25% of the BM (by volume), and >95% of the remaining space is located within 25 μm of the nearest blood vessel²⁴. Segmentation is therefore key to the accurate determination of the interstitial pH and $[Ca^{2+}]_e$ separately from the intravascular values that are systemically regulated. Moreover, the high cellular density reduces the interstitial space to a small fraction of the total BM volume, as confirmed by the fluorescence images of the cell-impermeable dyes showing the dark (unlabeled) cells filling most of the BM space. Ratiometric measurement would not be meaningful if the dark spaces filled by BM cells were included in the analysis (Suppl. Figure 2). The segmentation step

ensures that the ratiometric analysis is restricted to the narrow gaps between cells where the signals are detected.

With the developed methodology, we found the BM interstitial pH to be slightly lower (6.8-7.4, or 7.0-7.2, 10-90% confidence interval) than the serum (7.0-7.4, or 7.2-7.3, 10-90% confidence interval). We did not observe any location in the BM, including the endosteal surface of R-type cavities, where the pH falls below 6.8. This is consistent with the fact that small molecules, including the SNARF-1 pH sensor, are kept out of the tight seals between the osteoclasts and the bone resorption pits. Within the sealing zone, pH as low as 4.7 has been measured using an ion electrode inserted into this space¹¹. Even lower pH was found in vitro between cultured osteoclasts and their substrate. However when moving the electrode in the vicinity of the osteoclast outside the sealing zone, the pH was found to be in the physiologic range (7.0-7.2) and no pericellular pH gradient was observed, indicating that tight barrier is impermeable to even the smallest ions¹¹. Fluorescence imaging of local acidification under the resorbing osteoclasts was previously demonstrated using a pH sensor anchored to the bone matrix by conjugating it to a bisphosphonate group²⁵. Here we focus our analysis on the interstitial space rather than the sealing zone.

Quantification of the BM interstitial pH is an obligatory step toward measuring $[Ca^{2+}]_e$ because of the pH sensitivity of calcium indicators including Rhod-5N. We obtained calibration curves for Rhod-5N/AF488 ratio in response to calcium at pH 6.8, 7.0, and 7.4, corresponding to the range of pH values found in the steady state BM. We did not notice significant differences in the calibration at pH 7.0 and 7.4 ($p=0.23$), representing the majority of the interstitial space (Figure 1f). However, the K_{eff} for pH 6.8 was 19% lower than pH 7.0 and 7.4 (Suppl. Figure 6). The pH of 6.8 was the lowest value found in the BM and was rare in the steady state. However, it is possible that under inflammatory or other disease conditions^{26,27} the BM can become more acidic, and additional calibration curves will be required if measurements are to be extended to a lower pH range.

The most unexpected outcome of our ratiometric analysis is the absence of a strong calcium gradient toward the endosteal surface where bone resorption takes place. The BM has long been considered a calcium-rich microenvironment, as large quantities of calcium is stored in bone and liberated during bone resorption. How the calcium released from the bone is spatially distributed in the BM is not known. The tight seal between the osteoclast and the bone substrate is impermeable to both proton and calcium. It is also inaccessible to the pH and the calcium sensors. In the interstitial BM space where the sensors were distributed, the measured $[Ca^{2+}]_e$ was at a comparable level to the serum in both R- and M-type cavities (Figure 4b-c), whereas the level was significantly lower in D-type cavities. In all cases we did not find a steep increase in $[Ca^{2+}]_e$ toward the endosteal surface. Previous studies have shown that degraded bone matrix materials are transported through osteoclasts by transcytotic vesicular trafficking toward the functional secretory domain on the apical membrane facing away from the bone²⁸. The lack of a detectable $[Ca^{2+}]_e$ gradient in the BM suggests that free calcium ions may not be released directly into the interstitial fluid by the osteoclasts, although we cannot rule out the possibility that the release may be pulsatile and the transient increase is not captured in our imaging timeframe. It is also possible that the released calcium is strongly buffered. Bone remodeling is characterized as distinct phases involving bone resorption, a reversal stage, and bone formation. Such temporal evolution engages a dynamic transport of calcium ions out of the mineralized matrixes (resorption) followed by transport back into the osteoid during active bone formation via uni-directional transporters such as Na^+/Ca^{2+} exchangers expressed on the osteoblasts^{29,30}. We did observe very high $[Ca^{2+}]_e$ in osteoids on the endosteal surface of many D-type cavities, although how the calcium is transported from the osteoclast resorption sites to the osteoids remains to be investigated.

We have previously shown that in response to stimulation by cyclophosphamide and G-CSF, HSCs proliferated in a spatially heterogeneous manner. Expanding clusters were found exclusively in M-type cavities, while HSCs remain as single cells in D-type cavities⁷. Our current finding that D-type cavities had significantly lower interstitial calcium lends additional support to the concept that the hematopoietic microenvironment is different in distinct types of BM cavities undergoing various stages of bone turnover. Intriguingly, the most primitive LT-HSCs marked by *MDS1*^{GFP/+}; *Flt3*^{cre} were not found in BM locations with the lowest $[Ca^{2+}]_e$, in contrast to in vitro culture conditions where low environmental calcium was shown to reduce HSC mitochondrial calcium levels and improved HSC maintenance. Furthermore, the calcium-mitochondrial pathway was found to be critical in driving HSC division, and inhibition of calcium entry with a channel blocker also improved HSC maintenance in vitro^{3,6}. Collectively, these results point to the need to further examine the relationship between extracellular and intracellular calcium levels under in vivo conditions.

The major limitation of the present study is the need to pair the calcium indicator (Rhod-5N) with a reference dye (AF488) for ratiometric imaging. Although the two dyes have similar molecular weights, their tissue biodistribution may not be identical, resulting in uncertainty in the measured fluorescence ratio. In future studies, it will be preferable to conjugate both dyes to a carrier such as dextran with a fixed stoichiometry. Dextran conjugates have an additional benefit of longer imaging time window due to their slower rates of clearance.

To conclude, two-photon intravital imaging with ratiometric analysis enables quantifications of BM interstitial calcium and pH at high resolution. We found the depth correction to be essential and can be broadly applied to all ratiometric measurement performed through turbid media and tissue. More importantly, we found a moderate level of calcium in the BM interstitial space, with no sign of a strong calcium gradient toward the endosteal surface. In addition, we identified a relationship between bone remodeling and interstitial calcium concentration, with differing $[Ca^{2+}]_e$ among distinct types of BM cavities, and that primitive MFG LT-HSCs were not found at locations with lowest $[Ca^{2+}]_e$. This work thus paves a way for several important future directions, such as investigating the impacts of pH and interstitial calcium on HSCs under stressed conditions, and the communications between extra- and intracellular calcium, which will provide insight in therapeutic development towards modulation of calcium axis in the BM.

METHODS

Animals

For all experiments, 3- to 6-month-old adult male mice were used. We excluded female mice as serum calcium could be affected by estrogen fluctuations³¹. C57BL/6J mice were purchased from The Jackson Laboratory (Stock No. 000664). *MDS1*^{GFP/+}; *Flt3*^{Cre} mice were generously provided by Dr. Fernando Camargo (Boston Children's Hospital), bred in house, and genotyped following the protocols previously reported⁷. All experimental protocols were approved by the MGH Institutional Animal Care and Use Committee (IACUC approval 2007N000148), and experiments were conducted in compliance with the Guide for the Care and Use of Laboratory Animals.

Sample preparation for pH and calcium calibration in vitro

The pH clamping solution for establishing the calibration curve was prepared a day before imaging and stored in 4°C overnight. Samples were warmed to 37°C the next day for measurement. The pH clamping solution was based on FBS, supplemented with 10mM HEPES, 10mM MOPS, 4 mM KCl, 0.8 mM MgCl₂, CaCl₂ and EGTA adjusted to have 2 mM calcium, and NaCl adjusted to physiological concentration (154 mM). The pH meter (Mettler Toledo, FiveEasy™ FP20) was pre-

calibrated using pH 4, 7, 10 buffers. The calcium-pH clamping solution was also based on FBS, supplemented with 10mM HEPES, 10mM MES (pH 6.5), 4 mM KCl, 0.8 mM MgCl₂, and NaCl adjusted to physiological concentration (154 mM). pH values were adjusted to 6.8, 7.0, and 7.4, and then from the aliquots of a given pH, CaCl₂ and EGTA were supplemented to yield calcium concentrations between 0 to 40 mM. Of note, pH values could change during EGTA-Calcium reactions and when adding the pH or calcium indicators, pH of each sample was measured and adjusted to the target value right before fluorescence imaging and confirmed again immediately after image acquisitions.

To further validate the ratio of in vivo calcium imaging, whole blood was extracted by cardiac puncture and left at room temperature for coagulation (15 to 30 minutes), followed by centrifugation (2000g) at 4°C for 10 minutes. The supernatant (serum) was moved to a new tube immediately. The serum was then placed on ice throughout all preparation procedures and can be stored in the fridge for up to a week. As serum pH fluctuate significantly when exposed to air, pH of each sample was measured and adjusted to the target value right before fluorescence imaging. For all in vitro calibrations, glass slides were rinsed with 2 mM EGTA followed by dH₂O, and then air dried to remove calcium residuals on glass.

For pH measurements, 3.3 μL of SNARF-1 dextran 70kDa (D3304, ThermoFisher, 10 mg/mL in PBS) was added to 42 μL FBS-based serum samples based on the in vivo dose that yielded satisfactory contrast (110 μL, 44 mg/kg), assuming that the blood volume was 1400 μL. For calcium measurements, the mixture of Rhod-5N (R14207, ThermoFisher, 1 mM in dH₂O), AF488 (A33077, ThermoFisher, 0.5mg/mL in dH₂O), and sterile saline (5M) were also based on the dosage used in vivo (168 μL, 120 μL, 9 μL, respectively). Although it is based on approximation, it is important to note that trivial fluctuation in the working concentration would not alter the measured ratios (Suppl. Figure 4a-b). In the calibration curves, the true calcium concentrations of all samples were confirmed by the Arsenazo III assay (Pointe Scientific) following the vendor's protocol. In brief, a 10 μL sample was mixed with the Arsenazo III reagent to obtain its absorbance at 650 nm. The reference absorbance was measured with the standard calcium solution (2.5 mM, Pointe Scientific). [Ca²⁺] was then calculated by [2.5*sample absorbance/reference absorbance]. All measurements were performed on the same date of fluorescence measurements.

In vivo and in vitro image acquisitions

Intravital microscope was performed as previously described³². In brief, a femtosecond excitation laser beam was generated from an Insight X3 laser and was focused onto the sample through a 60x water-immersion objective (LUMFLN60XW). We used 8 mW power at the sample for all the in vitro experiments and the power was increased to 40 mW for in vivo measurements. An area of 200 μm by 400 μm was scanned for both in vivo and in vitro experiments with 500 x 1000 pixels corresponding to 0.4 μm per pixel. The fluorescence emissions and second harmonic generation from the bone were directed to the photomultiplier tubes with proper dichroic mirrors. Specifically, we used 370/100 nm bandpass filter to detect second harmonic generation of collagen. For pH imaging, we used 780 nm to excite SNARF-1 and the fluorescence emission at the green and red range were detected with 650/50 nm and 545/130 nm bandpass filters, respectively. For calcium imaging, we used 820 nm as the excitation wavelength and detected the fluorescence of Rhod-5N and AF488 using 607/70 nm and 525/50 nm bandpass filters, respectively. For bone remodeling imaging, we tuned the laser to 775 nm to excite Calcein Blue and Alizarin Red, which were detected in the blue channel with a 460/60 nm bandpass filter, and in the red channel with a 607/70 nm bandpass filter, respectively. All image stacks were acquired with a 3-μm step size from the calvaria surface, and 60 frames from the live scanning (30 fps) were averaged to acquire a single image.

In vitro calibrations

The serum and dye mixture prepared as described above were imaged at three randomly picked locations. The ratios of the fluorescence intensity centered at the 650nm to the fluorescence intensity at 545nm (defined as R/G ratios) were plotted as a function of pH to generate the pH calibration curve. The calibration curve was described as the following:

$$pH = pK_a + \log_{10} \left(\frac{R - R_0}{R_M - R} \right) + \log_{10} \left(\frac{S_{red,basic}}{S_{red,acid}} \right) \quad \text{Equation 1}$$

, where pK_a is the log form of acid dissociation constant, R is measured R/G ratios, R_0 is the R/G value at pH=5.8, R_M R/G value at pH=9.4, $S_{red,basic}$ is the SNARF-1 red emission at pH=9.4 and $S_{red,acid}$ is the SNARF-1 red emission at pH=5.8.

For in vitro calcium measurements, serum samples were prepared with calcium and pH clamping buffers as described above. We varied calcium concentration from 0mM to 40mM and adjusted their pH values to 6.8, 7 or 7.4. The final serum samples with different calcium concentrations and pH values were split into two, with a half measured with Arsenazo III to obtain true $[Ca^{2+}]$, and the other half for ratiometric quantifications. The ratio of Rhod-5N/AF488 (defined as Rhod-5N/AF488 ratio) were calculated from three random locations and was plotted against the calcium concentrations confirmed by the Arsenazo III assay. The Rhod-5N/AF488 ratios at corresponding calcium concentrations were obtained from 3 independent experiments. The data points were then fitted with Equation 2 to get the effective dissociation constant (K_{eff}).

$$[Ca^{2+}] = K_{eff} \times \left(\frac{R - R_0}{R_M - R} \right) \quad \text{Equation 2}$$

, where $[Ca^{2+}]$ is the calcium concentration, K_{eff} is effective dissociation constant, R is the measured Rhod-5N/AF488 ratios, R_0 is the ratio when calcium concentration is 0mM and R_M is ratio when calcium concentration is 40mM.

Of note, all in vitro calibrations were performed at 37C using a programmable thermo control pad secured on the microscope stage.

In vivo pH and calcium imaging

In vivo pH and calcium measurement procedures were approved by the Institutional Animal Care and Use Committee at Massachusetts General Hospital. Animals were anesthetized with an induction dose of 3% isoflurane and a maintenance dose of 1.25%. We removed the hair on the head and created a skin flap to expose the calvaria. The animals were secured in a heated mouse restrainer under the microscope for stable data acquisition. All the dyes were prepared freshly before each experiment. For pH measurements, 44 mg/Kg of SNARF-1 dextran (10 mg/mL in PBS) was delivered through retro-orbital injection. pH imaging typically started 10 minutes after dye administration to allow sufficient perfusion of the dextran dye to interstitial space. For calcium measurements, we implemented the following steps to ensure successful analytical corrections during post-processing in order to eliminate artifacts from optical loss and pharmacokinetic clearance. Specifically, we first located the targeted cavities and recorded their background noise and x-y coordinate before administering fluorescent probes. Then, 150 µg of Rhod-5N (168 µL in dH₂O) and 60 µg of Alexa Fluor 488 (120 µL in dH₂O) dye mixture were prepared with 32X saline solution (9 µL) and injected retro-orbitally. In vivo imaging on the chosen bone marrow cavities was performed immediately after injection. At each location, we took at least two stacks with 5- to 10-minute time interval in between in order to calculate the dye clearance rate. The animals were sacrificed under anesthesia after the experiment.

Lastly, to calibrate for the signal change due to dye preparation (e.g., pipetting errors or dye quality), a reference sample (from in vitro calibration) with known calcium concentration was mixed with the same dye mixture aliquoted from the in vivo trial and imaged immediately after the intravital calcium imaging. The Rhod-5N/AF488 ratios on different experiments was then corrected based on equation 3,

$$Ratio_M^{adj} = Ratio_M \times \frac{Ratio^{ref1}}{Ratio^{ref2}} \times \frac{(K_d^{-1} + [CaB^{ref1}]^{-1})}{(K_d^{-1} + [CaB^{ref2}]^{-1})} \quad \text{Equation 3}$$

, where $Ratio_M^{adj}$ is the calibrated Rhod-5N/AF488 ratio, $Ratio_M$ is the Rhod-5N/AF488 ratio before calibration, $Ratio^{ref1}$ is the measured ratio of the standard sample on day 1, $Ratio^{ref2}$ is the measured ratio of the standard sample after each in vivo experiments, K_d^{-1} is the dissociation constant of Rhod-5N, $[CaB^{ref1}]$ is the calcium concentration of the standard sample on day 1 and $[CaB^{ref2}]$ is the calcium concentration of the standard sample we imaged after each in vivo experiments (Suppl. Figure 7).

Bone remodeling imaging and classification

The rationales, protocols, and quantifications of bone remodeling imaging were detailed in our work published previously⁷. In brief, two calcium-binding dyes were administered sequentially. The first calcium-binding dye (Dye 1, Calcein Blue, Sigma, 30 mg/kg) was administered intraperitoneally 48 h before imaging to label and track the change of bone fronts over the course of 2 days, which approximately represents one cycle of bone resorption. Calcein Blue was chosen to be spectrally compatible with Rhod-5N and AF488. The second calcium-binding dye (Dye 2, Alizarin Red, 40 mg/kg) was administered after completing in vivo calcium imaging to label all the bone fronts. As Dye1 would be eroded if bone resorption has occurred, the Dye 1 to Dye 2 ratio in a single bone marrow cavity (the concave endosteum) indicates the stage of bone remodelling during the 48-h period. We then defined bone cavities as (i) deposition type (D-type; dye 1:dye 2 > 75%); (ii) resorption type (R-type; dye 1:dye 2 < 25%), and (iii) mixed type (M-type; dye 1:dye 2 between 25–75%.

Image processing

High resolution images were acquired using our intravital microscope as described. For all the images, we first subtracted background noise of each channel which was determined by a saline sample (in vitro) or the same field of view before dye administration (in vivo) taken under the same microscope configuration. The background-free image stacks were then analyzed in a custom-written Matlab code. In brief, we used the SHG signal from the bone structures and Otsu thresholding to generate bone masks. For fluorescence stacks, segmentation of vascular and interstitial space was performed using SNARF-1 red signal and Rhod-5N signal from pH and calcium imaging, respectively. We enhanced the image contrast of the red channel (either from the red emission of SNARF-1 or the emission from Rhod-5N) by using a histogram equalization and allowed 10% of the pixels being saturated. Next, we applied a top-hat filtering at each depth and eliminated uneven illumination in the image stacks. A local adaptive thresholding with Gaussian-weighted mean was used to generate masks of both the interstitial space and the vascular network. Of note, though Rhod-5N intensity fluctuates with calcium, low SNR regions can be picked up effectively using histogram equalization followed by image binarization based on adaptive local thresholding. Regions without Rhod-5N signals also lacked signals in the green channel, suggesting that the lack of Rhod-5N was due to optical attenuation or dye perfusion, not scarce $[Ca^{2+}]$. In addition, as fluorescence collected in the green channel contains significant amount of autofluorescence from bone and BM cells, segmentation based on the red channel excluded autofluorescence contamination easily. We also intentionally used an excitation

wavelength that favors Rhod-5N (820 nm) instead of AF488 (775nm) for calcium imaging in order to increase the dynamic range of measured ratios, thus the Rhod5N channel provided better image contrast and an overall more accurate segmentation result.

Two-step depth correction

Once obtaining the segmented vascular and interstitial maps, the depth correction of each acquisition channel is based on exponential attenuation of the fluorescence intensity with depth, shown in Eq. 4, where I is the measured intensity, I_0 is the original intensity, C_1 and C_2 are the attenuation coefficients from bone and bone marrow, respectively, subject to factors such as tissue optical properties of a given region and wavelengths; Z_1 and Z_2 are the bone thickness and the depth from endosteum, respectively. Therefore, the correction process includes two steps: (i) thickness correction, by determining C_1 and Z_1 . This step adjusts the fluorescence intensity in the bone marrow to the values without attenuation from the cortical bone (I'_0). (Eq. 5); (ii) depth correction: as the thickness-corrected stack is only subject to depth attenuation in the bone marrow, this step determines C_2 and Z_2 to recover the true fluorescence intensity, I_0 (Eq. 6). The processes of finding C_1 , C_2 , Z_1 , and Z_2 based on the acquired image stacks are detailed below.

$$I_0 = I/e^{-(C_1Z_1+C_2Z_2)} \quad \text{Eq. 4}$$

$$I/e^{-(C_1Z_1)} = I'_0 = I_0e^{-(C_2Z_2)} \quad \text{Eq. 5}$$

$$I_0 = I'_0/e^{-(C_2Z_2)} \quad \text{Eq. 6}$$

To obtain the bone thickness (Z_1) and the depth from endosteum (Z_2), segmentation of bone and bone marrow space was performed based on the second harmonic generation (SHG) of bone structures. The thickness map (M_t) is a 2D map where each pixel represents the bone thickness (Z_1) at a given x-y coordinate. The depth map (M_d) is a 3D stack where the value of any given pixel in the 3D bone marrow space indicates the distance to the endosteum (Z_2) of the same x-y coordinates (orthogonal to the horizontal plane).

To determine the attenuation coefficients of red and green fluorescence in bone (C_{1R} , C_{1G}), we first selected multiple regions from vessels located right at the endosteum, under an assumption that the ratios of these endosteal vessels are solely distorted by heterogenous bone thickness. Since the intravascular pH or calcium should remain constant, the correct combination of C_{1R} and C_{1G} , and the corresponding $I'_{0,R}$, $I'_{0,G}$ (Eq. 5) would converge the intravascular Rhod-5N/AF488 or SNARF1(R/G) ratios. Of note, there are multiple solutions of C_{1R} and C_{1G} combinations that would minimize the variation of intravascular ratios. Therefore, the attenuation of bone autofluorescence in the green channel was then used to determine a unique C_{1G} (Suppl. Figure 1b); subsequently, rendering a single solution of C_{1R} .

To determine the attenuation coefficients of red and green fluorescence in the bone marrow (C_{2R} , C_{2G}), we first segment the vessels (FIJI), and used customized matlab code to plot the mean intensity of vessels at each depth based on the thickness corrected stack (I'_0) and the depth map, M_d . The mean intensity at each depth was then corrected using Eq. 6 in an attempt to bring the intensity values back to the reference plane at the endosteum depth and minimize the standard deviation of the measured intensity. As a result, this two-step correction converges the intravascular ratios in the bone marrow.

Clearance correction

To compensate for signal loss due to dye clearance, we analyzed the stacks taken at the same location at different time points. The image stacks taken at two time points were first co-registered with FIJI (Descriptor-based 3D registration). Then, the aligned stacks were fed into a customized Matlab program that evaluated the decay rate for Rhod-5N and AF488 separately. For each dye, the images were first divided into 20-by-20-pixel subregions. The value of each subregion was

assigned with the mean intensity of the non-zero pixels. To acquire the decay rate, we fit the values of each subregion taken at two time points with a one-component exponential function. Lastly, both the Rhod-5N and AF488 intensities were corrected with the decay coefficient to 10 s after dye injection, assuming the 10 s as the time needed for tissue distribution.

Data analysis

Overall, the ratiometric map (Red/Green ratio) was obtained following these steps in sequence (i) pixel-by-pixel background subtraction based on the same field of view acquired before administering fluorescence probes, (ii) two-step depth correction (Figure 1), (iii) subtracting the signal crosstalk from each collection channel, and (iv) clearance correction (Suppl. Figure 4). Note that the signal crosstalk in each collection channel was obtained by labeling *in vitro* samples with just one fluorophore to retrieve the fraction of its fluorescence detected in the other channel. The signal crosstalk was therefore determined to be 12% (Rhod-5N leaked to the green channel) and 1.3% (AF488 leaked to the red channel). pH or calcium results were plotted by manually selecting random subregions within individual bone marrow cavities (approximately 5 μm x 5 μm or 20 μm x 20 μm for vessels and interstitial space, respectively). Manual selection was performed to avoid regions contaminated by saturated fluorescence at certain endosteal regions. For analyzing the calcium concentration near LT-HSCs, we manually selected four to five 3-cell radius interstitial neighborhood of each MFG cell, excluding intravascular space.

Statistics

A total of 10 mice were included for obtaining calcium distribution in association with bone remodeling. Four of the animals were *MDS1^{GFP/+};Flt3^{cre}* and were used to acquire calcium microenvironment adjacent to 7 MFG cells. Depending on the size of each cavity, 10 - 25 subregions were randomly chosen for statistical analysis. Statistically significant difference was evaluated using two-tailed Mann-Whitney U test (Prism8, GraphPad) and the results were presented with mean +/- standard deviation.

DATA AVAILABILITY

All data needed to evaluate the conclusions in the paper are present in the paper and the Supplementary Materials and will be available from the corresponding author on reasonable request.

REFERENCES

1. Adams, G. B. et al. Stem cell engraftment at the endosteal niche is specified by the calcium-sensing receptor. *Nature* 439, 599–603 (2006).
2. Peacock, M. Calcium metabolism in health and disease. *Clin J Am Soc Nephrol* 5, 23–30 (2010).
3. Luchsinger, L. L. et al. Harnessing hematopoietic stem cell low intracellular calcium improves their maintenance *in vitro*. *Cell Stem Cell* 25, 225–240 (2019).
4. Tordoff, M. G., Bachmanov, A. A. & Reed, D. R. Forty mouse strain survey of voluntary calcium intake, blood calcium, and bone mineral content. *Physiol Behav* 91, 632–643 (2007).
5. Jafri, L., Habib, A. & Saba, K. Ionized calcium measurement in serum and plasma by ion selective electrodes : comparison of measured and calculated parameters. *Ind J Clin Biochem* 29, 327–332 (2014).
6. Umemoto, T., Hashimoto, M., Matsumura, T., Ishizu, A. N. & Suda, T. Ca²⁺ – mitochondria axis drives cell division in hematopoietic stem cells. *J. Exp. Med.* 215, 2097–2113 (2018).

7. Christodoulou, C. et al. Live-animal imaging of native haematopoietic stem and progenitor cells. *Nature* 578, (2020).
8. Tsien, R. Y. & Rink, T. J. Neutral carrier ion-selective microelectrodes for measurement of intracellular free calcium. *Biochem. Biophys. Acta* 599, 623–638 (1980).
9. Meyerhoff, M. E. & Fraticelll, Y. M. Ion-selective electrodes. *Anal. Chem.* 54, 27R-44R (1982).
10. Nicholson, C., Bruggencate, G. Ten, Steinberg, R. & Stockle, H. Calcium modulation in brain extracellular microenvironment demonstrated with ion-selective micropipette. *Proc. Natl. Acad. Sci. USA* 74, 1287–1290 (1977).
11. Silver, I. A., Murrills, R. J. & Etherington, D. J. Microelectrode studies on the acid microenvironment adherent macrophages and osteoclasts. *Exp Cell Res* 175, 266–276 (1988).
12. Stosiek, C., Garaschuk, O., Holthoff, K. & Konnerth, A. In vivo two-photon calcium imaging of neuronal networks. *Proc. Natl. Acad. Sci. USA* 100, 7319–7324 (2003).
13. Bonhoeffer, T. et al. Highly ordered arrangement of single neurons in orientation pinwheels. *Nature* 442, 925–928 (2006).
14. Kinase, N. et al. TRPM7 activates m-calpain by stress-dependent stimulation of p38 MAPK and c-Jun N-Terminal kinase. *J Mol. Biol.* 396, 858–869 (2010).
15. Grewe, B. F., Langer, D., Kasper, H., Kampa, B. M. & Helmchen, F. High-speed in vivo calcium imaging reveals neuronal network activity with near-millisecond precision. *Nat. Methods* 7, 399–405 (2010).
16. Lutche, H. et al. Optical recording of neuronal activity with a genetically- encoded calcium indicator in anesthetized and freely moving mice. *Front. Neural Circuits* 4, 1–12 (2010).
17. Gao, M. et al. Aggregation-induced emission probe for light-up and in situ detection of calcium ions at high concentration. *ACS Appl. Mater. Interfaces* 10, 14410–14417 (2018).
18. Sui, B., Liu, X., Wang, M. & Belfield, K. D. A highly selective fluorescence turn-on sensor for extracellular calcium ion detection. *Chem. Eur. J.* 22, 10351–10354 (2016).
19. Rusakov, D. A. & Fine, A. Extracellular Ca²⁺ depletion contributes to fast activity-dependent modulation of synaptic transmission in the brain. *Neuron* 37, 287–297 (2003).
20. Narayanaswamy, N. et al. A pH-correctable, DNA-based fluorescent reporter for organellar calcium. *Nat. Methods* 16, 95–102 (2019).
21. Constantinides, C., Mean, R. & Janssen, J. J. Effects of isoflurane anesthesia on the cardiovascular function of the C57BL/6 Mouse Christakis. *ILAR J.* 52, 21–31 (2011).
22. Itkin, T. et al. Distinct bone marrow blood vessels differentially regulate haematopoiesis. *Nature* 532, 323–328 (2016).
23. Salmon, J., Vigo, J. & Goyet, C. Measurements of calcium with a fluorescent probe Rhod-5N : Influence of high ionic strength and pH. *Talanta* 71, 437–442 (2007).
24. Spencer, J. a et al. Direct measurement of local oxygen concentration in the bone marrow of live animals. *Nature* 508, 269–73 (2014).
25. Maeda, H. et al. Real-time intravital imaging of pH variation associated with osteoclast activity. *Nat. Chem. Biol.* 12, 579–585 (2016).
26. Linden, C. Vander & Corbet, C. Therapeutic targeting of cancer stem cells : integrating and exploiting the acidic niche. *Front. Oncol.* 9, 1–12 (2019).
27. Casimir, G. J. The acid – base balance and gender in Inflammation : a mini-review. *Front. Immunol.* 9, 1–6 (2018).
28. Salo, J., Lehenkari, P., Mulari, M. & Metsikko, K. Removal of osteoclast bone resorption products by transcytosis. *Science* (80-). 276, 270–273 (1997).
29. Blair, H. C. et al. Osteoblast differentiation and bone matrix formation in vivo and in vitro. *Tissue Eng. Part B* 23, 268–280 (2017).
30. Stains, J. P., Weber, J. A. & Gay, C. V. Expression of Na⁺/ Ca²⁺ exchanger isoforms (NCX1 and NCX3) and plasma membrane Ca²⁺ ATPase during osteoblast differentiation. *J. Cell. Biochem.* 84, 625–635 (2002).

31. Voznesenskaya, A. & Tordoff, M. G. Influence of estrous and circadian cycles on calcium intake of the rat. *Physiol Behav.* 112, 56–60 (2013).
32. Lo Celso, C. et al. Live-animal tracking of individual haematopoietic stem/progenitor cells in their niche. *Nature* 457, 92–6 (2009).

ACKNOWLEDGEMENT

We thank Lin laboratory members for discussions and Dr. F. Camargo (Boston Children's Hospital) for providing MDS1^{GFP}; FLT3^{cre} mice. This study was supported by awards from the National Institute of Health (R01 DK123216 and P01 HL142494 to C.P.L.).

AUTHOR CONTRIBUTIONS

S.-C.A.Y., J.H, and C.P.L designed the experiments. S.-C.A.Y. and J.H, performed the experiments and data analysis. J.W. assisted in data analysis relevant to image processing. S.-C.A.Y., J.H, and C.P.L. wrote the manuscript. C.P.L. supervised the project and gave final approval.

COMPETING INTERESTS

The authors declare that they have no competing interests.

Figures

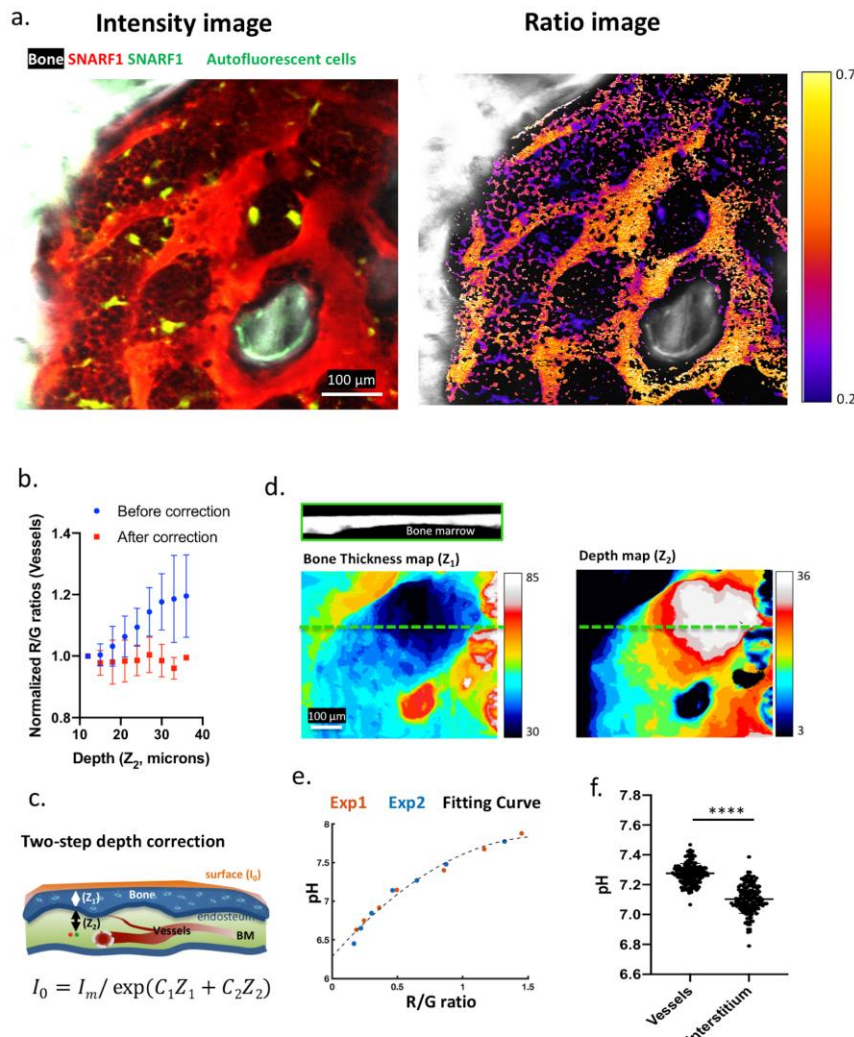


Figure 1. Ratiometric imaging of bone marrow pH in vivo. (A) SNARF-1 fluorescence intensity and ratio images of a single optical section from a z-stack (shown in Suppl. Video 1). The cell impermeable SNARF-1 dextran labeled the vasculature and the interstitial space. The BM cells thus appeared as dark objects. (B) The mean of SNARF-1 (R/G) ratios obtained from vessels located at various distances to endosteum (depths). Without correction, the R/G ratio increased with increasing image depth. After correction for the wavelength-dependent light attenuation, the intravascular R/G ratio became independent of depth ($n = 6$ bone marrow cavities). (C) Schematic illustration of the two-step depth correction. Fluorescence signals originated in the BM travel through BM and bone with distinct attenuation coefficients ($C_{1,2}$) before being collected by the objective lens. (D) Bone thickness shows varying thickness across the field of view. The corresponding depth map shows varying distances to endosteum from a single z plane. The cross-section view corresponds to an x-z section from the green dashed line. (E) A pH calibration curve obtained in vitro to convert measured ratios to absolute pH ($N=2$ independent experiments, 3 measurements were performed on each in vitro sample). (F) Ratiometric quantification of intravascular and interstitial pH after the two-step depth correction. Interstitial pH was found to be significantly lower than intravascular pH, with 10% - 90% data points distributed between 7.0-7.2. Each data point represents a subregion from a bone marrow cavity ($n= 10$ cavities, $N= 2$ mice). *** $P < 0.0001$; two-sided Mann-Whitney test. Mean \pm s.d.

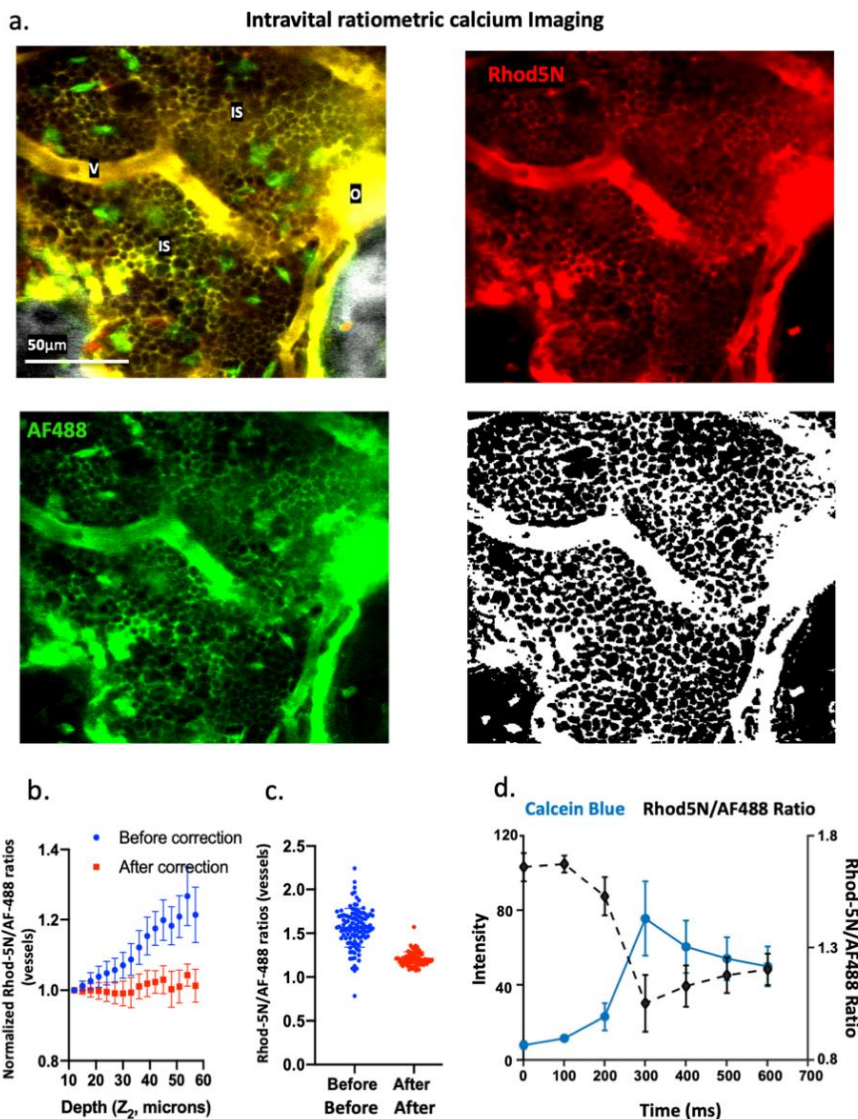


Figure 2. Ratiometric calcium imaging of bone marrow. (A) Intravital two-photon fluorescence imaging of BM cavities labeled with Rhod-5N (red) and AF488 (green). The SHG signal from bone is shown in gray. The mask for interstitium and vessels were generated from Rhod-5N images to delineate the vasculature and the interstitial space while excluding areas with low fluorescence signals (i.e. intracellular space that is not labeled by the cell-impermeable dye). Autofluorescent cells are also excluded. V: vessels; IS: interstitium; O: Osteoids. (B) The mean of Rhod-5N/AF488 ratios obtained from vessels located at various distances to endosteum (depths), showing a consistent increase in the Rhod5-N/AF488 ratios with increasing image depth. Correction for depth attenuation of Rhod-5N and AF488 signals independently yielded intravascular ratios independent of depth ($n = 6$ bone marrow cavities). (C) Ratiometric analyses without the two-step depth correction yielded divergent intravascular Rhod-5N/AF488 ratios, while depth corrections minimized variation of intravascular ratios. (D) Real-time response of the Rhod-5N/AF488 ratio (black circles) during the injection of a calcium chelator, Calcein Blue (blue squares). Each data point represents the mean of 5 subregions from the blood vessels. Mean \pm s.d.

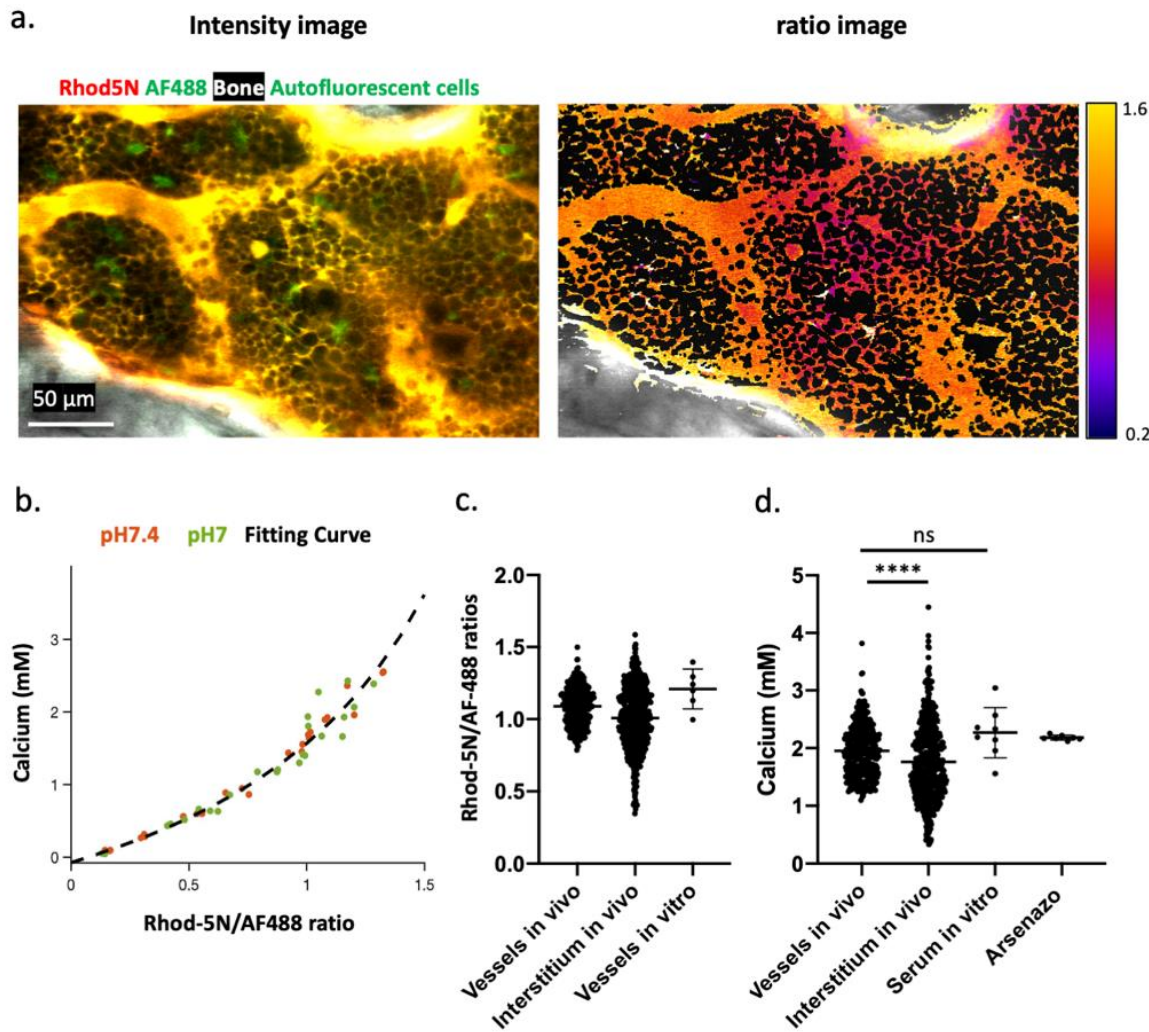


Figure 3. Quantification of intravascular and interstitial calcium concentration in the bone marrow. (A) Merged Rhod-5N, AF488 and SHG signals and ratiometric imaging in the bone marrow, demonstrated by a single image plane from a z-stack. Rhod-5N and AF488 as cell impermeable dyes labeled vasculature and were sequestered in the interstitial space. The bone marrow cells thus appeared as dark objects. (B) Calcium concentration calibration curves at pH= 7.0 and pH=7.4 were obtained in vitro to convert the measured ratios to absolute calcium concentration (N=3 independent experiments, 6 measurements were performed on each in vitro sample). The dashed black line is a fitting curve for two data sets together with $K_{\text{eff}} = 2.6$ for pH=7.0 and pH=7.4. (C) Quantifications of intravascular and interstitial Rhod-5N/AF488 ratios in vivo as well as serum Rhod-5N/AF488 ratios measured in vitro. (D) Corresponding calcium concentrations converted from Rhod-5N/AF488 ratios in (C) using the calcium calibration curve, compared to the serum calcium measured by Arsenazo III assay from the same animals (N= 7 out of 10) undergoing in vivo measurements. Each data point represents a subregion from a bone marrow cavity (n= 14 cavities, N= 10 mice). ****P < 0.0001, two-sided Mann–Whitney test. Mean \pm s.d.

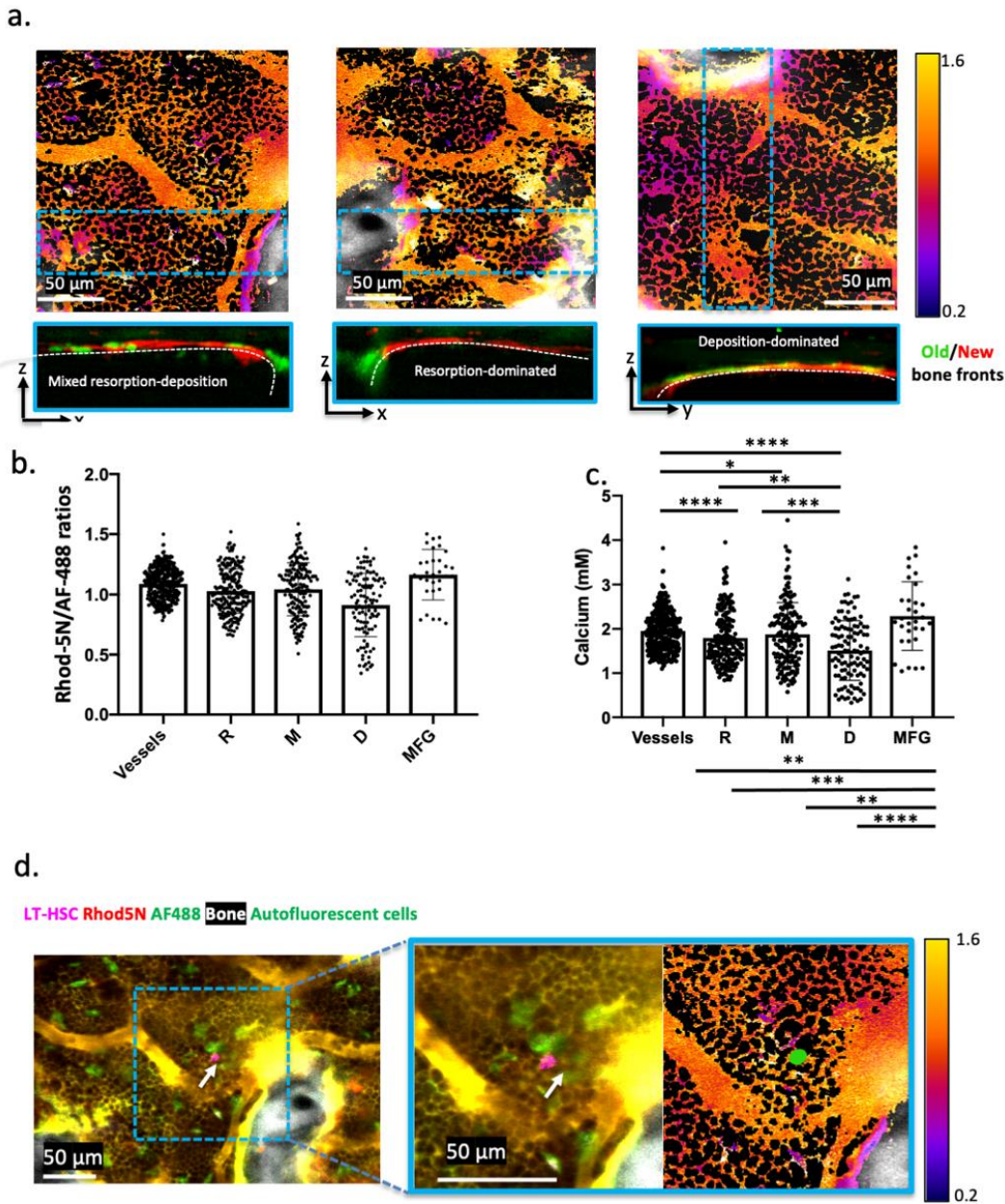


Figure 4. Quantitative calcium measurements in different cavity types and HSC microenvironment. (A) Ratiometric imaging of Rhod-5N/AF488 from BM cavities dominated by bone deposition (D-type), resorption (R-type), or mixed activities (M-type). Bone remodeling is defined by the double calcium staining strategy⁷ based on the Dye1/Dye2 ratio, where Dye1 labels the old bone fronts that has been eroded to various extents. The cross-section view of bone remodeling from a BM cavity is obtained from the x-z or y-z sections of the blue dashed zone, displayed by maximum intensity projection. (B-C) Quantifications of intravascular and interstitial Rhod-5N/AF488 ratios in D-, M-, R-type cavities and near LT-HSCs, together with the corresponding calcium concentrations converted from ratiometric analyses. Each data point represents a subregion from a bone marrow cavity ($n= 14$ cavities, $N= 10$ mice). **** $P < 0.0001$; *** $P < 0.001$; ** $P < 0.01$; * $P < 0.05$, two-sided Mann–Whitney test. Mean \pm s.d. (D) A representative image of Rhod-5N/AF488 labeled bone marrow in *MDS1*^{GFP/+},*FLT3*^{Cre} mice used to measure interstitial calcium adjacent to GFP+ LT-HSCs.

Figures

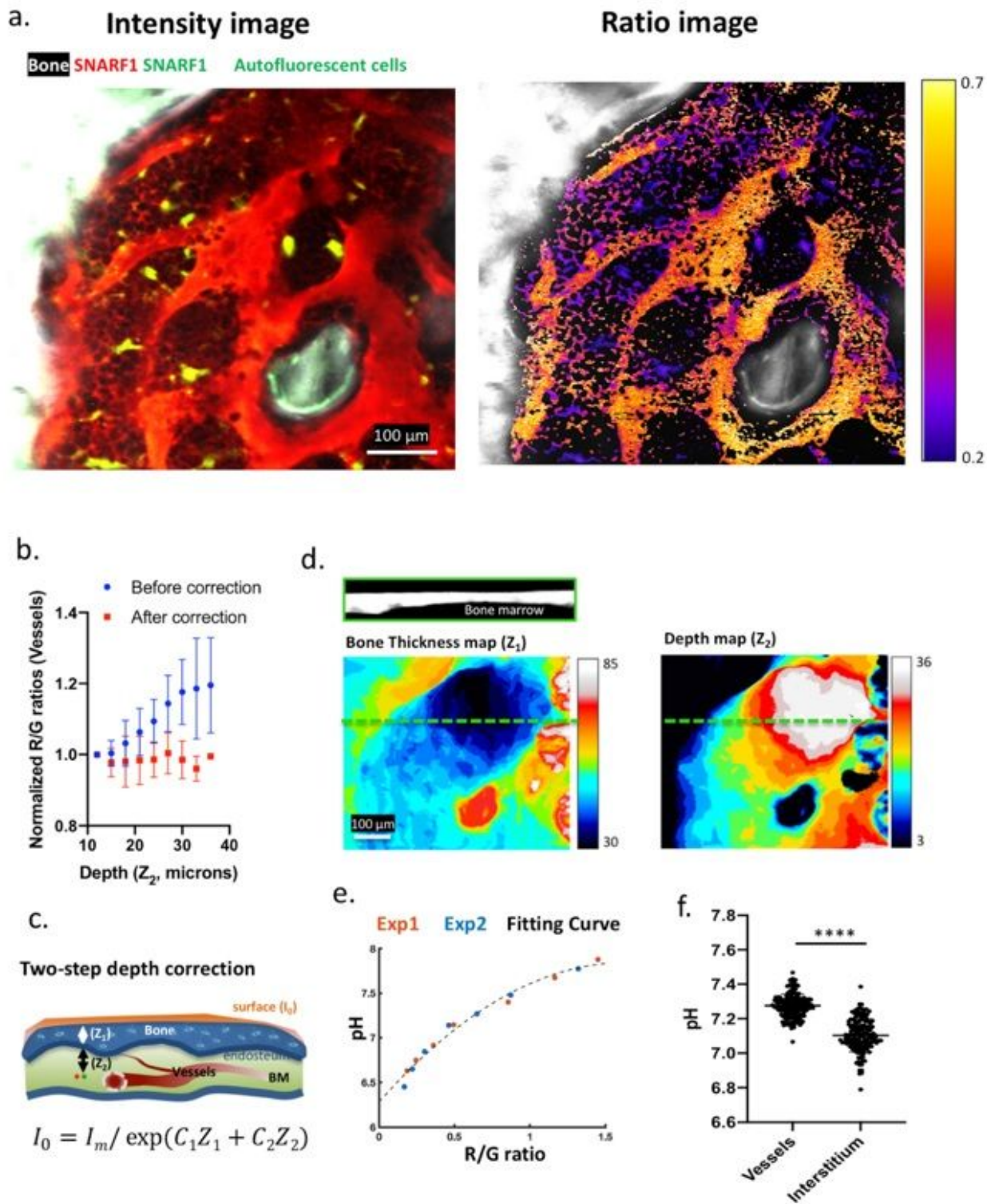


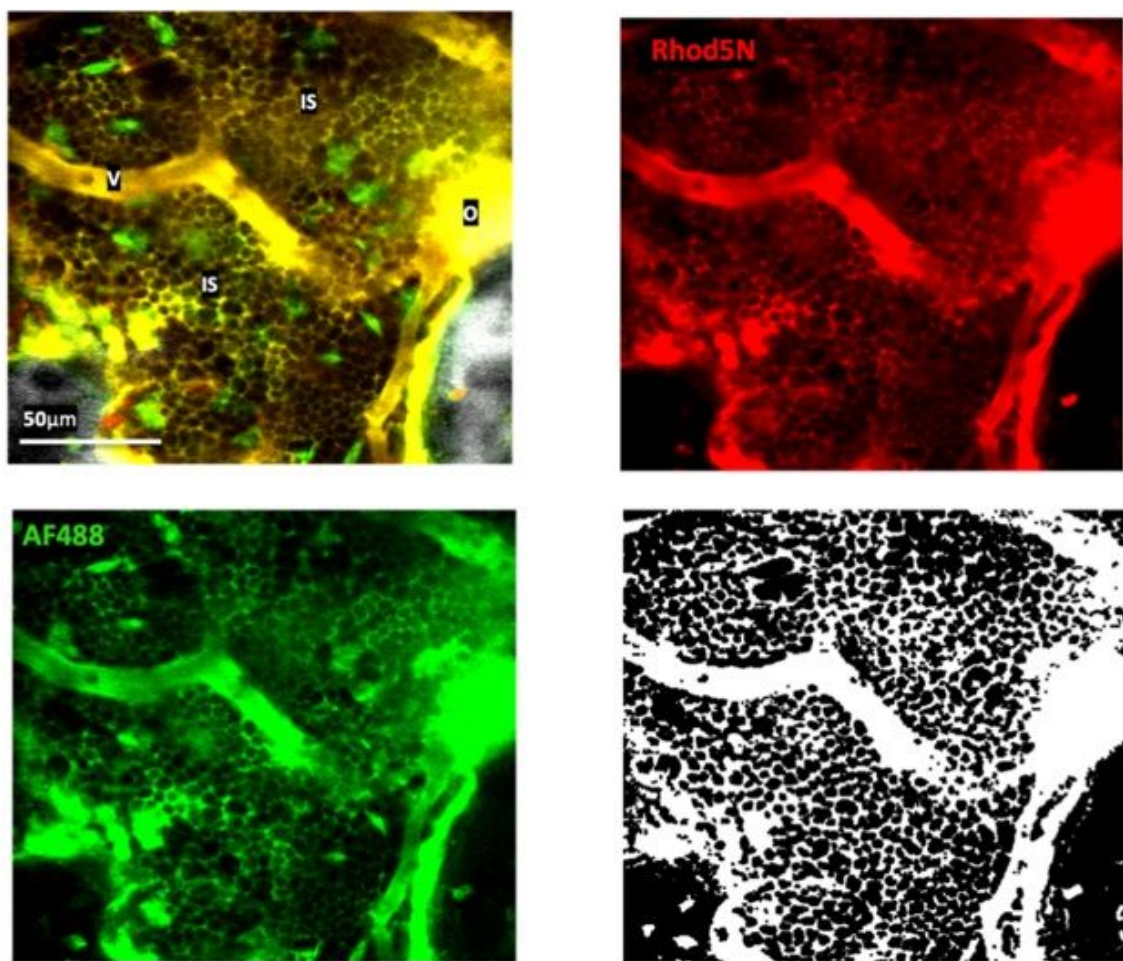
Figure 1

Ratiometric imaging of bone marrow pH *in vivo*. (A) SNARF-1 fluorescence intensity and ratio images of a single optical section from a z-stack (shown in Suppl. Video 1). The cell impermeable SNARF-1 dextran labeled the vasculature and the interstitial space. The BM cells thus appeared as dark objects. (B) The

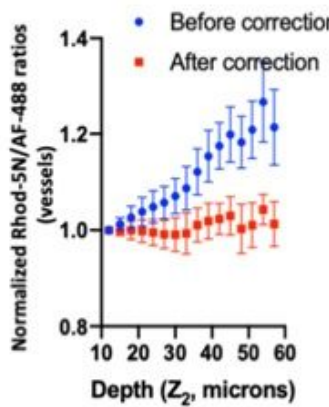
mean of SNARF-1 (R/G) ratios obtained from vessels located at various distances to endosteum (depths). Without correction, the R/G ratio increased with increasing image depth. After correction for the wavelength-dependent light attenuation, the intravascular R/G ratio became independent of depth ($n = 6$ bone marrow cavities). (C) Schematic illustration of the two-step depth correction. Fluorescence signals originated in the BM travel through BM and bone with distinct attenuation coefficients (C_{1,2}) before being collected by the objective lens. (D) Bone thickness shows varying thickness across the field of view. The corresponding depth map shows varying distances to endosteum from a single z plane. The cross-section view corresponds to an x-z section from the green dashed line. (E) A pH calibration curve obtained in vitro to convert measured ratios to absolute pH (N=2 independent experiments, 3 measurements were performed on each in vitro sample). (F) Ratiometric quantification of intravascular and interstitial pH after the two-step depth correction. Interstitial pH was found to be significantly lower than intravascular pH, with 10% - 90% data points distributed between 7.0-7.2. Each data point represents a subregion from a bone marrow cavity ($n= 10$ cavities, N= 2 mice). ****P < 0.0001; two-sided Mann–Whitney test. Mean ± s.d.

a.

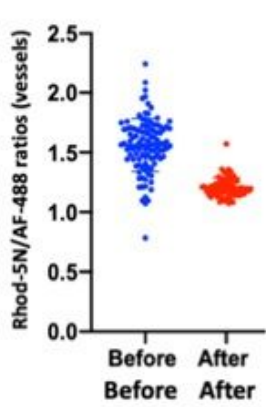
Intravital ratiometric calcium Imaging



b.



c.



d.

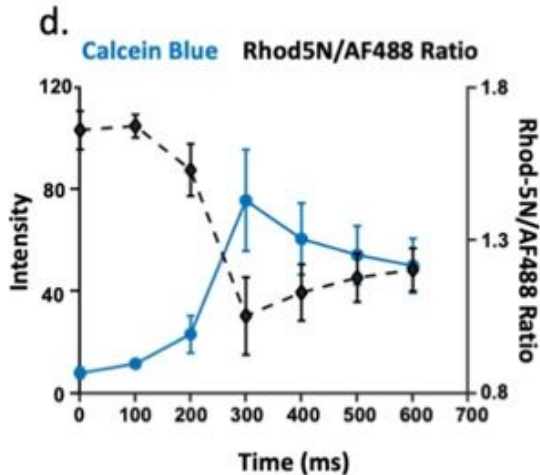


Figure 2

Ratiometric calcium imaging of bone marrow. (A) Intravital two-photon fluorescence imaging of BM cavities labeled with Rhod-5N (red) and AF488 (green). The SHG signal from bone is shown in gray. The mask for interstitium and vessels were generated from Rhod-5N images to delineate the vasculature and the interstitial space while excluding areas with low fluorescence signals (i.e. intracellular space that is not labeled by the cell-impermeable dye). Autofluorescent cells are also excluded. V: vessels; IS:

interstitium; O: Osteoids. (B) The mean of Rhod-5N/AF488 ratios obtained from vessels located at various distances to endosteum (depths), showing a consistent increase in the Rhod-5N/AF488 ratios with increasing image depth. Correction for depth attenuation of Rhod-5N and AF488 signals independently yielded intravascular ratios independent of depth ($n = 6$ bone marrow cavities). (C) Ratiometric analyses without the two-step depth correction yielded divergent intravascular Rhod-5N/AF488 ratios, while depth corrections minimized variation of intravascular ratios. (D) Real-time response of the Rhod-5N/AF488 ratio (black circles) during the injection of a calcium chelator, Calcein Blue (blue squares). Each data point represents the mean of 5 subregion from the blood vessels. Mean \pm s.d.

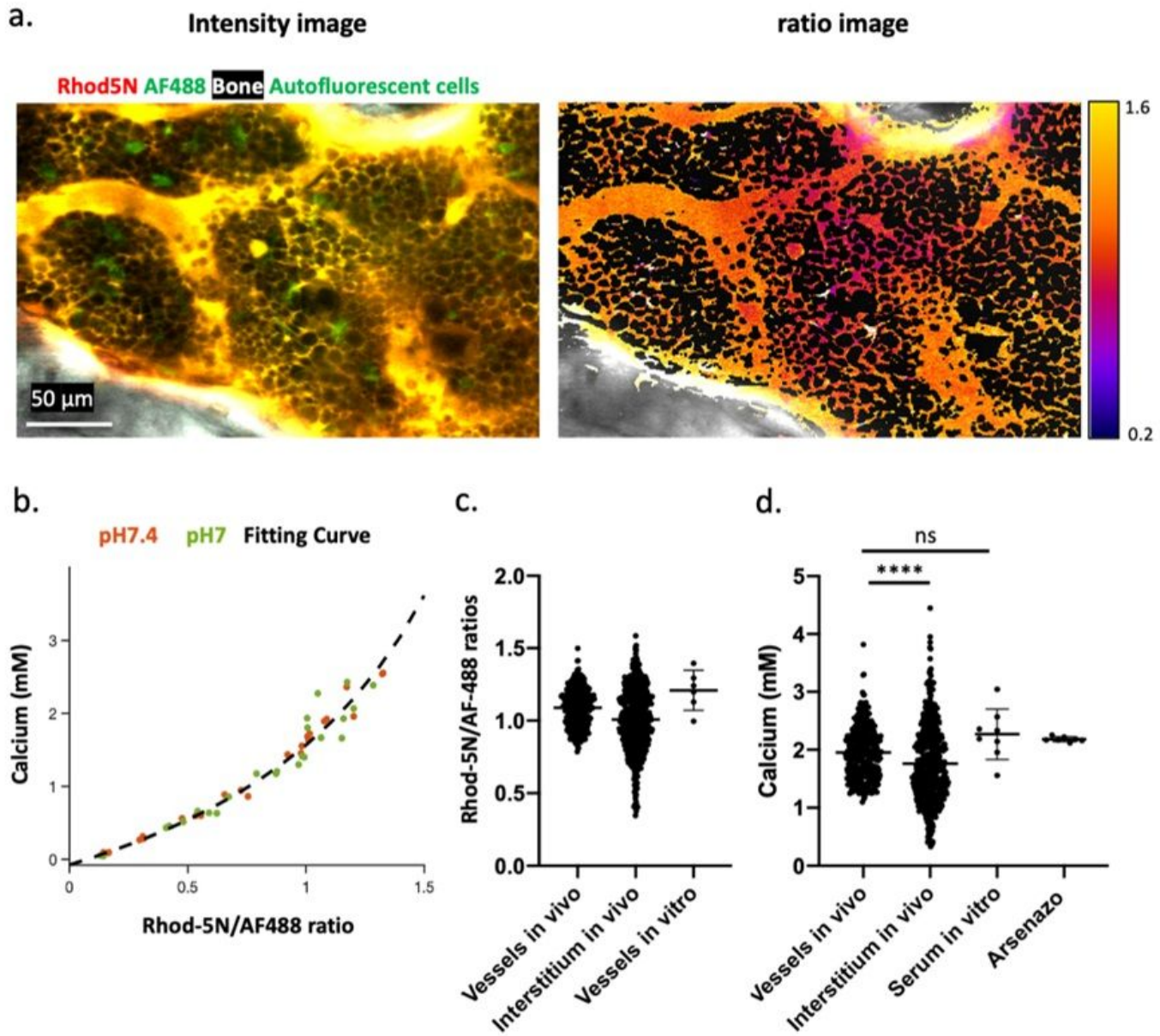
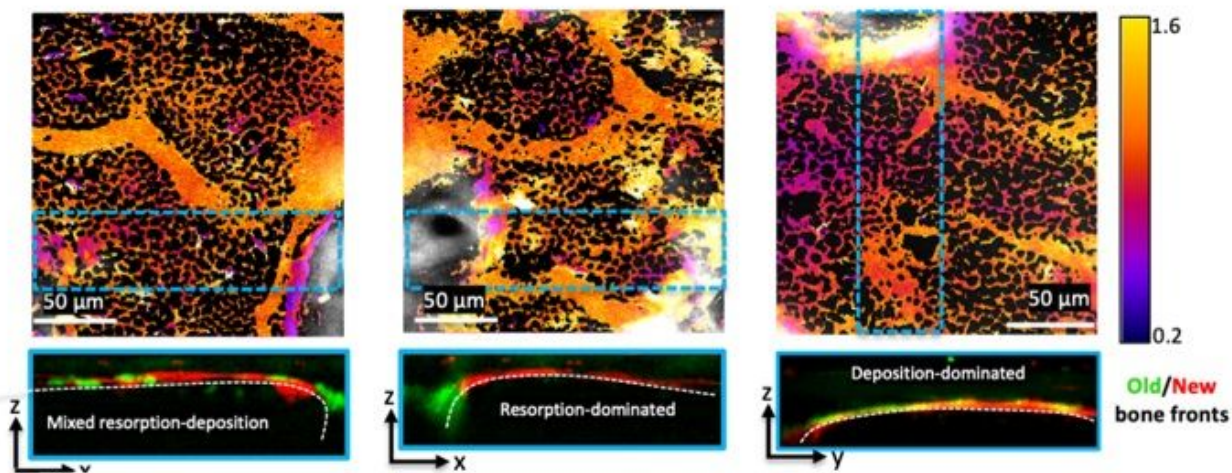


Figure 3

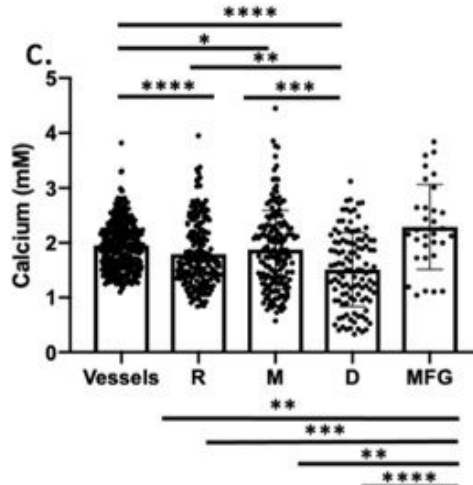
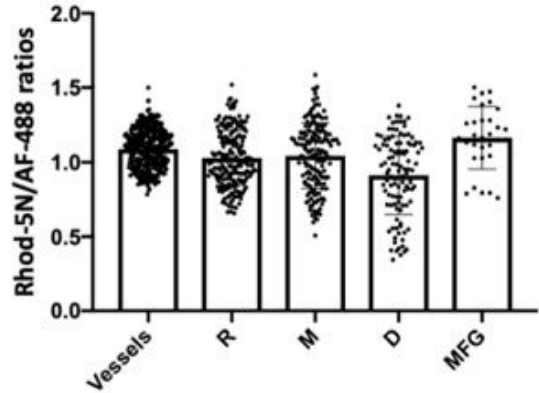
Quantification of intravascular and interstitial calcium concentration in the bone marrow. (A) Merged Rhod-5N, AF488 and SHG signals and ratiometric imaging in the bone marrow, demonstrated by a single

image plane from a z-stack. Rhod-5N and AF488 as cell impermeable dyes labeled vasculature and were sequestered in the interstitial space. The bone marrow cells thus appeared as dark objects. (B) Calcium concentration calibration curves at pH= 7.0 and pH=7.4 were obtained in vitro to convert the measured ratios to absolute calcium concentration (N=3 independent experiments, 6 measurements were performed on each in vitro sample). The dashed black line is a fitting curve for two data sets together with $K_{eff} = 2.6$ for pH=7.0 and pH=7.4. (C) Quantifications of intravascular and interstitial Rhod-5N/AF488 ratios in vivo as well as serum Rhod-5N/AF488 ratios measured in vitro. (D) Corresponding calcium concentrations converted from Rhod-5N/AF488 ratios in (C) using the calcium calibration curve, compared to the serum calcium measured by Arsenazo III assay from the same animals (N= 7 out of 10) undergoing in vivo measurements. Each data point represents a subregion from a bone marrow cavity (n= 14 cavities, N= 10 mice). ****P < 0.0001, two-sided Mann–Whitney test. Mean \pm s.d.

a.



b.



d.

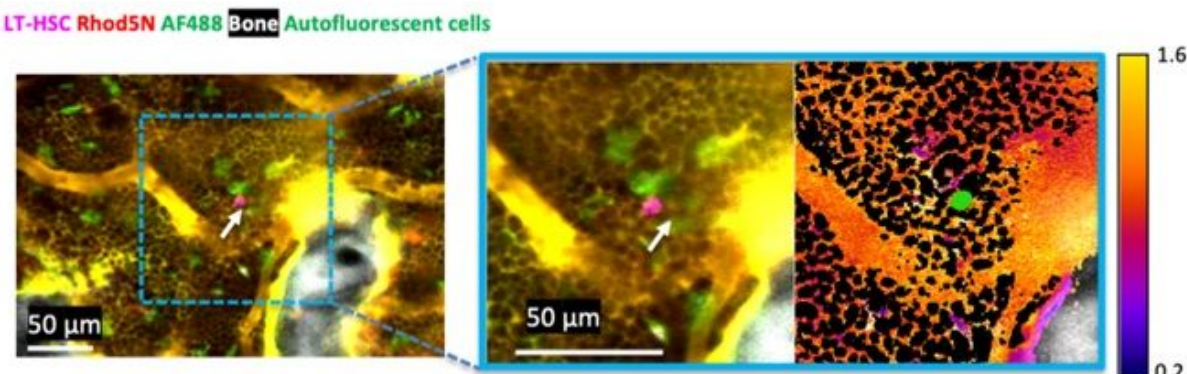


Figure 4

Quantitative calcium measurements in different cavity types and HSC microenvironment. (A) Ratiometric imaging of Rhod-5N/AF488 from BM cavities dominated by bone deposition (D-type), resorption (R-type), or mixed activities (M-type). Bone remodeling is defined by the double calcium staining strategy⁷ based on the Dye1/Dye2 ratio, where Dye1 labels the old bone fronts that has been eroded to various extents. The cross-section view of bone remodeling from a BM cavity is obtained from the x-z or y-z sections of

the blue dashed zone, displayed by maximum intensity projection. (B-C) Quantifications of intravascular and interstitial Rhod-5N/AF488 ratios in D-, M-, R-type cavities and near LT-HSCs, together with the corresponding calcium concentrations converted from ratiometric analyses. Each data point represents a subregion from a bone marrow cavity (n= 14 cavities, N= 10 mice). ****P < 0.0001; ***P < 0.001; **P < 0.01; *P < 0.05, two-sided Mann–Whitney test. Mean ± s.d. (D) A representative image of Rhod-5N/AF488 labeled bone marrow in MDS1GFP/+;FLT3Cre mice used to measure interstitial calcium adjacent to GFP+ LT-HSCs.

Supplementary Files

This is a list of supplementary files associated with this preprint. Click to download.

- [Video1withscalebarConverted.mov](#)
- [Video2withscalebarConverted.mov](#)
- [Video3withscalebarConverted.mov](#)
- [Video4withscalebarConverted.mov](#)
- [Video5annotatedwithscalebarConverted.mov](#)
- [Video6revisedannotatedwithscalebarConverted.mov](#)
- [NatCommSlvFinal.docx](#)